Nuclear Engineering and Technology 55 (2023) 2380–2387

Contents lists available at ScienceDirect

Nuclear Engineering and Technology

journal homepage: www.elsevier.com/locate/net

Original Article

The radiation shielding competence and imaging spectroscopic based studies of Iron ore region of Kozhikode district, Kerala

S. Arivazhagan [a], K.A. Naseer [b, c, *], K.A. Mahmoud [d], S.A. Bassam [b], P.N. Naseef Mohammed [b], N.K. Libeesh [a], A.S. Sachana [e], M.I. Sayyed [f, g], Mohammed S. Alqahtani [h, i, j], E. El Shiekh [h], Mayeen Uddin Khandaker [k]

[a] Centre for Applied Geology, The Gandhigram Rural Institute- Deemed to be University, Gandhigram, Dindigul, 624302, India
[b] Department of Physics, Farook College (Autonomous), Kozhikode, 673632, India
[c] MEU Research Unit, Middle East University, Amman, Jordan
[d] Ural Federal University, St. Mira, 19, 620002, Yekaterinburg, Russia
[e] Planetary Sciences Division, Physical Research Laboratory, Ahmedabad, 380059, India
[f] Department of Physics, Faculty of Science, Isra University, Amman, Jordan
[g] Department of Nuclear Medicine Research, Institute for Research and Medical Consultations (IRMC), Imam Abdulrahman bin Faisal University (IAU), P.O. Box 1982, Dammam, 31441, Saudi Arabia
[h] Research Center for Advance Materials (RCAMS), King Khalid University, Abha, 61421, Saudi Arabia
[i] Department of Radiological Sciences, College of Applied Medical Sciences, King Khalid University, Abha, 61421, Saudi Arabia
[j] BioImaging Unit, Space Research Centre, Department of Physics and Astronomy, University of Leicester, Leicester, LE1 7RH, United Kingdom
[k] Center for Applied Physics and Radiation Technologies, School of Engineering and Technology, Sunway University, 47500, Bandar Sunway, Selangor, Malaysia

ARTICLE INFO

Article history:
Received 2 February 2023
Received in revised form
21 March 2023
Accepted 29 March 2023
Available online 2 June 2023

Keywords:
Radiation shielding
Building materials
Iron ore and its associated rocks
MAC
HVL

ABSTRACT

Hyperspectral data and its ability to explore the minerals and their associated rocks have a remarkable application in mineral exploration and lithological characterization. The present study aims to explore the radiation shielding aspects of the iron ore in Kerala with the aid of the Hyperion hyperspectral dataset. The reflectance-spectra obtained from the laboratory conditions as well as from the image show various absorptions. The results from the spectra are validated with geochemical data and GPS points. The Monte Carlo simulation employed to evaluate the radiation shielding ability. Raising the oxygen ions caused a noteworthy decrease in the μ values of the studied rocks which is accompanied by an increase in $\Delta_{0.5}$ and Δ_{eq} values. The $\Delta_{0.5}$ and Δ_{eq} values increased by factors of approximately 77 % with raising the oxygen ions between 44.32 and 47.57 wt.%. The μ values varies with the oxygen concentrations, where the μ values decreased from 2.531 to 0.925 cm^{-1} (at 0.059 MeV), from 0.381to 0.215 cm^{-1} (at 0.662 MeV), and from 0.279 to 0.158 cm^{-1} (at 1.25 MeV) with raising the oxygen ions from 44.32 to 47.43 wt.%.

1. Introduction

Taking advantage of fuel sources to substitute manual and creature work was the strategy of Modernization: a time of extraordinary monetary and social turn of events. The hurriedly expanding total populace requests a massive measure of energy in the ongoing century. A large portion of the traditional energy sources is supplanted by nuclear reactors. Nuclear innovation is a blade that cuts both ways while thinking about the fallout. Many gamble factors are engaged with atomic innovation; including the potential weaknesses of nuclear criticality and various radiations are produced while the energy is created with nuclear power. The rich experience of the most recent decades had worked on the well-being of atomic influence creation, and the dangers are lessening. The focal point of support behind this is the hunger for new methods for security measures. Radiation safeguarding is the pith of dangerous radiation emanation and could be serious nervousness in different atomic power stations [1]. The exploration for enhanced radiation protection materials is going on diverse materials like alloys [2–5], composites [6–9], solutions [10], biomaterials [11], rocks [12,13], and amorphous materials [14–17].

* Corresponding author. Department of Physics, Farook College (Autonomous), Kozhikode, 673632, India.
E-mail address: naseerka.phy6@gmail.com (K.A. Naseer).

https://doi.org/10.1016/j.net.2023.03.038

The effectiveness of these materials could be checked using a range of interaction characteristics, including linear attenuation coefficient, mass attenuation coefficient, effective atomic number, etc. Due to the ease with which the desired size and shape may be produced, concretes are the conventional methods of radiation shielding. Additionally, this concrete must be thick and include heavy metals to provide radiation shielding. It is preferable to locate some alternate building materials due to the expense of using such vast volumes of heavy concretes. When blended with conventional concretes, the native rocks might hold traces of various materials that could be employed to block ionizing radiation. This is the scientific relevance of comparing the effectiveness of different types of rocks as radiation shields. This work consists of radiation safeguard investigations of several naturally occurring rocks from Kerala, an Indian state. We are approaching the problem from a new angle by considering how the materials themselves can defend the radiation. Some of the earlier efforts were based on the radioactivity of the building supplies themselves because of their contents [18].

Hyperspectral systems are the recent trend in remote sensing technology that has the characteristics of providing an image to a spectrum [19]. Unlike other broad-brand remote sensing systems like Landsat-TM and ASTER that considerably under-sample the reflectance data, hyperspectral sensors offer near laboratory quality reflectance data which can be utilized to differentiate materials based on their unique spectral signatures [20]. The Hyperion hyperspectral satellite was launched with the basic aim, to evaluate a space-based imaging spectrometer's capabilities for Geoscience and Earth observation operations with distinctive spatial, spectral, and temporal properties that are not currently available [21]. The Hyperion data have 242 spectral bands in between 360 nm to 2580 nm range (Visible and Infrared region of electromagnetic spectrum) with global coverage and launched as a part of NASA's New Millennium Program launched on 21st Nov 2000 [20]. A broad number of studies have utilized the discrimination capabilities of space-borne hyperspectral data such as Hyperion for extensive mineral as well as lithological mapping and discrimination and so on [22]. The previous studies conducted in the area reveal that the iron content of the formation is around 30–50% with Fe content dominantly belonging to oxide and sulfide iron ore classes (Magnetite, Hematite & Chalcopyrite) [23]. The major oxides values of the representative samples are given in Table 1. The present study investigate the capabilities of iron ore and its associated rocks in the radiation shielding application and its spatial extend demarcation through imaging spectroscopic aspects.

2. Materials and methods

The study area map is prepared by using the toposheet from the Survey of India and overlay with false color composition from Hyperion data (Fig. 1a). The geology map of the area is prepared using the freely available shape file from the Geological Survey of India website (Fig. 1b). Based on the map and random sampling method, the rock samples are collected and scrutinized to find out representative samples. Among them, magnetite, HBG, and charnockite are selected as the representative sample. The major oxides present in the representative sample were identified through XRF analysis (Table .1). The laboratory-based reflectance spectra were taken by using ASD Field Spec 4 High-Resolution Spectroradiometer in the wavelength range of 350 nm–2500 nm subsequently. The density of the rock samples was noted based on the method given in [24,25]. The cloud-free Hyperion Level 1-R imagery (Product ID: EO1H1450522007049110PZ) captured on Feb 23^{rd,} 2007 was gathered from USGS Earth Explorer. The pre-processing methods were performed on the data to remove the errors by using the ENVI software. Before that, the VNIR-SWIR bands of the Hyperion L1-R data set were layer stacked to remove the band bands. Further, the data were radiometrically calibrated and georeferenced, and co-registered using Hyperion L1GsT data (UTM/WGS 1984 zone 43N) of the same area. Then the geo-rectified image was atmospherically corrected using the FLASH algorithm.

Table 1
Major oxide (XRF) composition (wt.%) of HBG, Charnockite, and Magnetite rocks.

Major oxide data (XRF)	Rock type		
	HBG	Magnetite	Charnockite
SiO_2	62.71	58.08	64.68
TiO_2	0.85	0.62	0.55
Al_2O_3	14.8	3.11	13.48
MnO	0.18	0.12	0.16
Fe_2O_3	8.38	35.85	6.57
CaO	5.34	0.37	5.69
MgO	2.95	0.68	3.48
Na_2O	3.16	0.17	2.97
K_2O	0.45	0	1.28
P_2O_5	0.28	0.16	0.19
Density	**2.80**	**5.0**	**3.0**

3. Results and discussion

3.1. Image processing techniques

Color composites are used to express the color intensity variations by means of assigning different bands together in basic filters red, green, and blue for displaying the lithological variations or rock alterations [12,26]. The false-color composite image was derived by using the bands 42, 23, 13, in which the iron ore deposits shown in green color and the HBG and charnockite seen in the rose and cyan color respectively (Fig. 1a). Principal Component Analysis (PCA) is an exploratory analysis to enhance the image by selecting the maximum spectral contrast of all the bands and which makes use of the characterization properties [27]. Whereas, the Minimum Noise Fraction (MNF) is considered as an overhaul of the PCA technique which will be performed as a two-step process. The de-correlation and rescaling were done to the bands as a first step and altogether it is known as noise whitening. Subsequently, the PC image was obtained [28]. Band ratio is a statistical approach that will be performed based on the ratio of two different bands to a single band to enhance the spectral character [29]. It can be very much useful for enhancing the features that cannot be identified from the raw bands of the data [12]. Various band color composites were generated, among them, selected band color composites that are highlighting the iron ore that is represented here. The band ratio band combinations 57/22, 19/28, and 38/5 were used to discriminate the boundaries of litho units and the band combination provided good discrimination results. According to band combinations 57/22, 19/28, and 38/5 enhanced HBG in orange color, charnockite in yellow color, and iron ore in brown color (Fig. 2a). The PC bands of 7, 17, 42 that represent HBG in violet color, charnockite in green color, and iron ore deposits in rose color (Fig. 2b). MNF derived using the Hyperion bands 5, 9, 2 and the HBG has shown in cyan color, charnockite in green, and iron ore in pink color (Fig. 2c).

3.2. Spectral characterization

Recent studies are exploited to prospect the reflectance spectral response of minerals on the Earth and other planetary mineral investigation [30]. The properties of reflected or scattered lights to record the chemical content of the object as the function of wavelength were utilized in this kind of study. The vibrational and electronic processes are considered to be the main causes of the

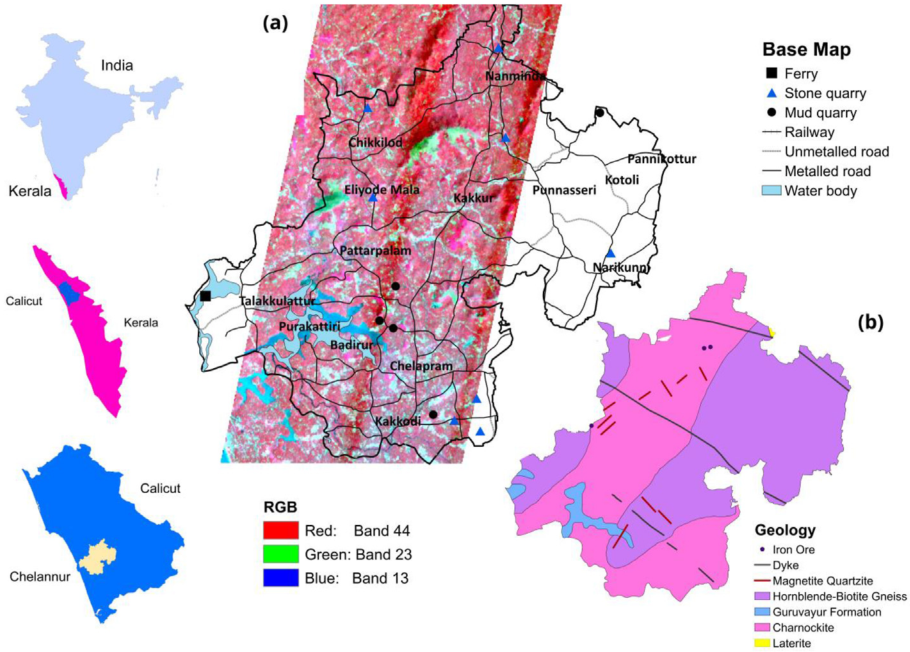

Fig. 1. (a) Base map of the study area overlaid in the False-color composite prepared by utilizing Hyperion bands 44, 23, and 13 in RGB filter. Iron ore deposits are shown in deep green color. HBG and charnockite are seen in the rose and cyan color respectively; (b) The geology map of the study area prepared using the shapefile given by GSI. (For interpretation of the references to color in this figure legend, the reader is referred to the Web version of this article.)

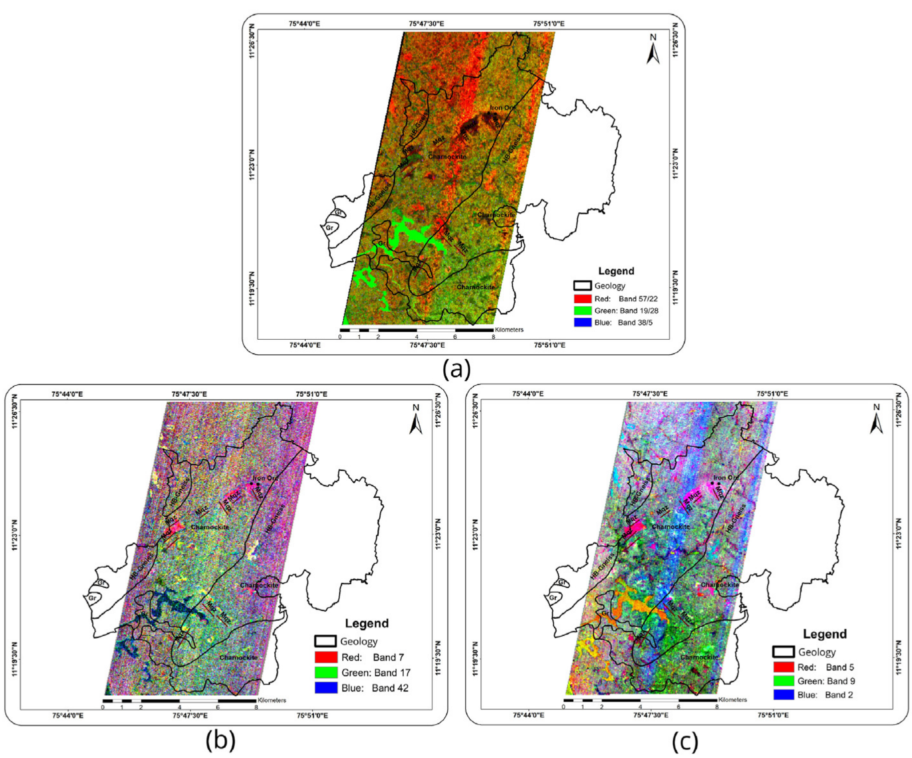

Fig. 2. (a) Hyperion Band ratios 57/22, 19/28, and 38/5 in RGB filter. HBG and charnockite are represented in orange and yellowish colors respectively. Iron ore is represented in brown color; (b) PCA derived Hyperion bands 7, 17, and 42 in RGB filter. Hornblende- Biotite Gneiss is shown in violet color and green color represents charnockite. Iron ore is indicated in rose color; (c) MNF derived Hyperion bands 5, 9, 2 in RGB. Hornblende-biotite gneiss is shown in cyan color, Charnockite in green & Iron ore in deep pink color. (For interpretation of the references to color in this figure legend, the reader is referred to the Web version of this article.)

absorption characteristics and which would be more evident in the visible and infrared portions of electromagnetic radiation [31]. The spectra representing iron ore (magnetite), HBG, and charnockite were derived from laboratory conditions (Fig. 3A) and Hyperion data (Fig. 3 B) based on ground truth data collected during the field survey. The spectra show prominent absorption features at 480 nm,

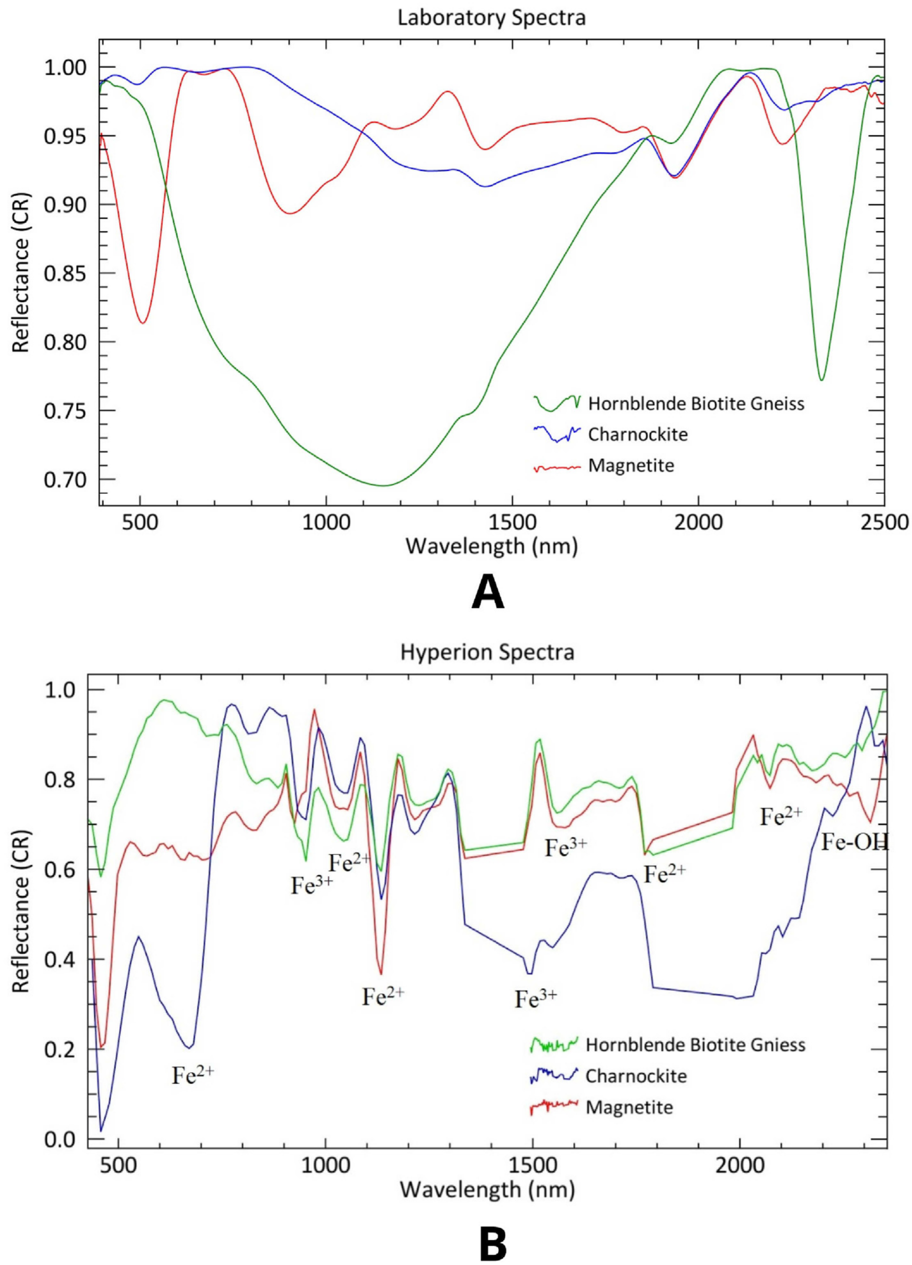

Fig. 3. (A) Laboratory spectra of HBG, Charnockite and Magnetite in the range of 350 nm–2500 nm; **(B)** Spectra were taken from the Hyperion image in the range of 350 nm–2500 nm.

700 nm, 850 nm–950nm, 1000 nm–1150nm, 1200 nm–1300nm, 1400 nm, 1500 nm, 1700 nm–2100nm, 2200 nm, and 2330 nm due to the absorptions of plagioclase UV absorption presence of Fe^{3+} ion, Fe^{2+} - Fe^{3+} electron transition, Fe^{3+}, Fe^{2+}, Fe^{2+} /Plagioclase, OH/Mn^{3+} crystal transition, Fe^{3+}, Fe^{2+}, Fe–OH and Mg–OH respectively [19,32–35]. The absorption features were a good correlation with the geochemical data shown in Table 1.

3.3. Radiation shielding features

The mass attenuation coefficient (μ_m, cm^2/g) for HBS, Magnetite, and Charnockite rocks was estimated using the Monte Carlo simulation in the E_γ values lie between 0.015 and 2.506 MeV. The variation of the μ_m values against the γ-photon energy has three various modes related to the type of γ-photon interaction, photoelectric (PE), Compton scattering (CS), and pair production (PP) interaction [36–38], as presented in Fig. 4a, b, and c. Fig. 4a describes the reduction of the μm values versus the low γ-photon energies between 0.015 and 0.122 MeV. The μm suffers a high reduction in the width raising the photon energy due to the PE cross-section that varies inversely with $E_\gamma^{3.5}$. In the mentioned energy interval, the μm loses approximately about 98.3 5 % (for HBS), 99.0 % (for Magnetite), and 98.3 % (for Charnockite), when the γ-photon energy increased from 0.015 to 0.122 MeV. In the intermediate E_γ values where the CS is the main interaction, Fig. 4b shows a reasonable reduction in the μ_m values by raising the E_γ among 0.122 MeV and 0.964 MeV. For example, the μ_m values were reduced approximately by a factor of 36.7 % (for HBS), 37.3 % (for Magnetite), and 36.6 % (for Charnockite). The mentioned moderate reduction is endorsed to the CS cross-section which varies inversely

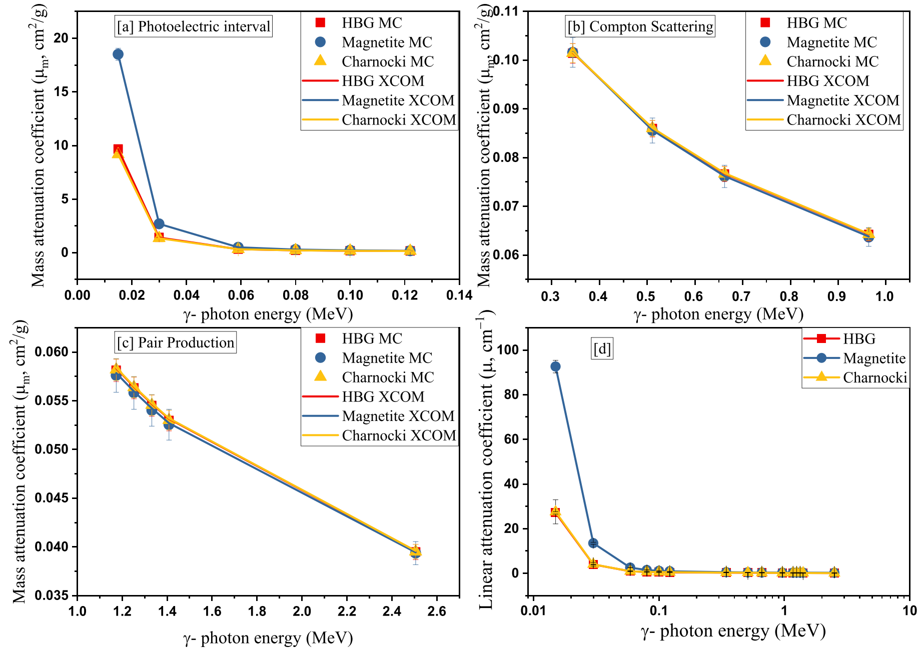

Fig. 4. Variation of the mass attenuation coefficient (μ_m, cm^2/g) and the linear attenuation coefficient (μ, cm^{-1}) versus the γ-photon energy (MeV).

with E_γ. In the third high E_γ interval which lies between 1.173 and 2.506 MeV, the μ_m values show a low dependence on the E_γ due to the PP cross-section with vary with log (E_γ). For example, Fig. 4c shows a slight reduction of the μ_m from 0.0581 to 0.0395 cm^2/g (for HBS), from 0.0576 cm^2/g to 0.0394 (for Magnetite), and from 0.0582 to 0.0395 cm^2/g (for Charnockite) associated with raising the E_γ values between 1.173 and 2.506 MeV. Moreover, the linear attenuation coefficient (μ, cm^{-1}) values for the investigated rocks are also simulated and presented in Fig. 4d, where the μ values have the same reduction trend as the μm values versus the incident E_γ values but the μ values decreased from 27.078 to 0.111 cm^{-1} (for HBS), from 92.550 to 0.197 cm^{-1} (for Magnetite) and from 27.519 to 0.119 cm^{-1} (for Charnockite) when E_γ values raised from 0.015 to 2.506 MeV.

Furthermore, the chemical composition illustrated in Table 1 shows a strong relation between Fe^{3+} and oxygen concentrations and the simulated μ values, as illustrated in Fig. 5. Fig. 5a shows an enhancement of the μ values with raising the Fe^{3+} concentrations. The mentioned enhancement is approximately about 63.4 %, 43.6 %, and 43.5 % at E_γ values of 0.059, 0.662, and 1.25 MeV, respectively. The results show a high enhancement in the μ values at low E_γ values followed by moderate enhancement in the μ values at intermediate E_γ values (i.e., 0.662 MeV) and high E_γ values (i.e., 1.250 MeV). The discussed behaviors are attributed to the relative to the interaction cross-section and the effective atomic number (Z_{eff}) of investigated rocks where the interaction cross-section varied with $(Z_{eff})^{4\text{-}5}$, Z_{eff}, and $(Z_{eff})^2$ for PE, CS, and PP interactions. The Z_{eff} of the investigated rocks is affected by the Fe^{3+} concentration, where raising the Fe^{3+} ions in the rock samples increases significantly the electron density, density, and the Z_{eff} of the investigated rocks which enhances the μ values of the presented rocks. In contrast, Fig. 5b shows a reduction in the μ values with an elevation in the oxygen concentrations, where the μ values decreased from 2.531 to 0.925 cm^{-1} (at 0.059 MeV), from 0.381to

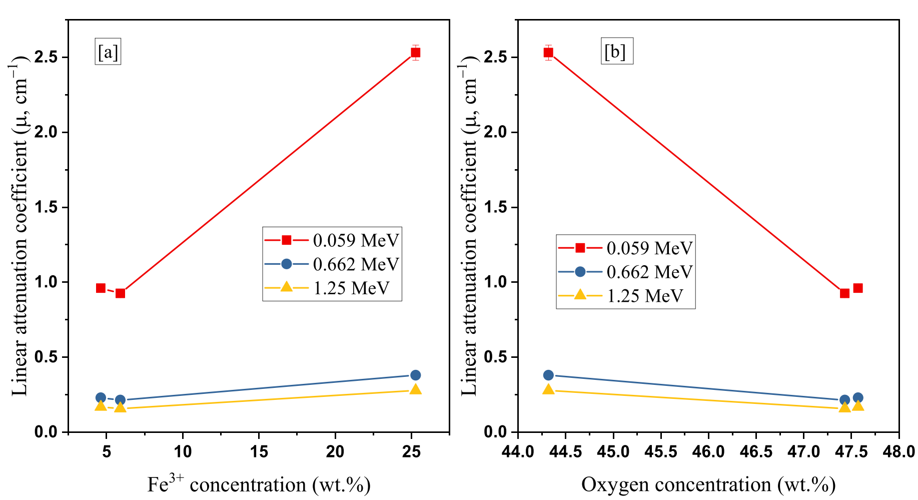

Fig. 5. Variation of the linear attenuation coefficient (μ, cm^{-1}) versus the Fe^{3+} and oxygen concentrations (wt.%).

0.215 cm^{-1} (at 0.662 MeV) and from 0.279 to 0.158 cm^{-1} (at 1.25 MeV) with raising the oxygen ions from 44.32 to 47.43 wt. %, respectively.

The thickness of the studied rock samples essential to absorb 50 % of the incident γ-photons is known as the half-value thickness ($\Delta_{0.5}$, cm) while the thickness of the rock samples which have the same γ-ray shielding capacity of pure lead (Pb) is known as the thickness equivalent (Δ_{eq}, cm) [39–42]. The variation of $\Delta_{0.5}$ and Δ_{eq} versus the incident E_γ values, as illustrated in Fig. 6 for the studied rocks HBG and Magnetite. The $\Delta_{0.5}$ values raised from 0.03 to 6.27 cm (for HBG), and from 0.01 to 3.52 cm (for Magnetite) by raising the E_γ photons from 0.015 to 2.506 MeV. The illustrated increase strongly in the low E_γ values followed by a moderate increase in the intermediate and high E_γ values owing to the interaction modes PE, CS, and PP. In contrast, the Δ_{eq} values were decreased for both HBG and Magnetite samples with raising the E_γ values. For example, the Δ_{eq} decreased from 46.53 to 4.44 cm (for HBG) and from 13.61 to 2.50 cm (for Magnetite), raising the E_γ values between 0.015 and 2.506 MeV. The decrease is strong in the low E_γ due to the high decrease in the Pb and studied rocks' μ values in the stated energy interval. After that, the Δ_{eq} values slowly decrease in the intermediate and high E_γ values due to the high reduction in Pb's μ values compared to the reduction achieved in the μ values for HBG and Magnetite rocks where the μ values decreased by factors of 85.8 %, 61.1 %, and 61.3 % for Pb, HBG, and Magnetite respectively when the E_γ increased between 0.122 and 2.506 MeV. In the low E_γ values, the Δ_{eq} for the studied rock samples suffers two followed increases at E_γ values of approximately 0.015 and 0.08 MeV due to the L and K edges of Pb in which the Pb's μ values increased to high values compared to the studied rocks' μ values.

The Fe^{3+} ions and oxygen concentrations also affected the values of $\Delta_{0.5}$, and Δ_{eq}, as illustrated in Fig. 7 a and b. Fig. 7a showed a decrease in the Δ_{eq} and $\Delta_{0.5}$ values with raising the Fe^{3+} concentration where the $\Delta_{0.5}$ values reduced from 3.23 cm to 1.82 cm and the Δ_{eq} values decreased from 5.79 cm to 3.27 cm with raising the Fe^{3+} ions concentration from 4.63 to 25.28 wt.%. The presented results showed that raising the Fe^{3+} concentration increases the resistance of the studied rocks to passing the energetic photons. Thus, an increase in the studied rocks' μ values is achieved. Hence, the $\Delta_{0.5}$ values are inversely varied with μ (i.e., $\Delta_{0.5} = 0.693/\mu$), so $\Delta_{0.5}$ decreased with raising the μ values. Also, the studied rocks' μ values showed an increase compared to the Pb's μ value. Thus, the Δ_{eq} decreased regard with to raising the Fe^{3+} concentration. In contrast, the $\Delta_{0.5}$ and Δ_{eq} values increased with raising the oxygen concentration in the fabricated rock samples, as illustrated in Fig. 7b. Raising the oxygen ions causes a significant decrease in the μ values of the studied rocks which is accompanied by an increase in $\Delta_{0.5}$ and Δ_{eq} values. The $\Delta_{0.5}$ and Δ_{eq} values increased by factors of approximately 77 % with raising the oxygen ions between 44.32 and 47.57 wt.%.

The transmission factor (TF, %) portrays the photons penetrating a given thickness of the studied rocks to the total number of incident photons in the studied rocks while the radiation protection efficiency (RPE, %) measures the number of absorbed photons inside a given thickness of the studied rocks to the total number of incident photons [43–45]. In the present study, the effect of γ-photon energy and the thickness of the studied rocks on the calculated values of TF and RPE are studied, as presented in Figs. 8 and 9. Fig. 8 describes the variation of TF and RPE versus the incident E_γ values. Raising the E_γ values decreases the photon wavelength which results in enhanced penetration power of the incident photons. Then, the photons penetrate the given thickness of the studied rock with a small number of collisions between photons and the surrounding electrons. Therefore, the amount of energy consumed by the passing photons decreased accompanied by an increase in the number of transmitted photons. Thus, the TF values increased accompanied by a significant decrease in the RPE values. For example, a thickness of 1 cm from the Magnetite mineral has a TF value raised from <1% to 82.2 % accompanied by a decrease in the RPE from ≈100 % to 17.9 % by raising the E_γ values from 0.105 to 2.506 MeV.

Furthermore, Fig. 9 illustrates the effect of the studied samples' thickness on the estimated values of TF and RPE values. The estimated results refer that the TF values decreased accompanied by an increase in the RPE values with raising the sample thickness. For example, growing the sample thickness between 0.5 and 10 cm causes a considerable decrease in the TF values from 82.7% to 2.2 % while the RPE rose from 17.3 % to 97.8 %, at the E_γ value of 0.662 MeV. Growing the sample thickness higher than the MFP of the studied samples causes an increase in the number of interactions between the γ-photons and the surrounding electrons. Therefore, the amount of energy consumed inside the sample layer increased accompanied by a considerable decrease in the number of transmitted photons. Thus, the RPE increase is accompanied by an increase in the RPE with growing the studied sample thickness.

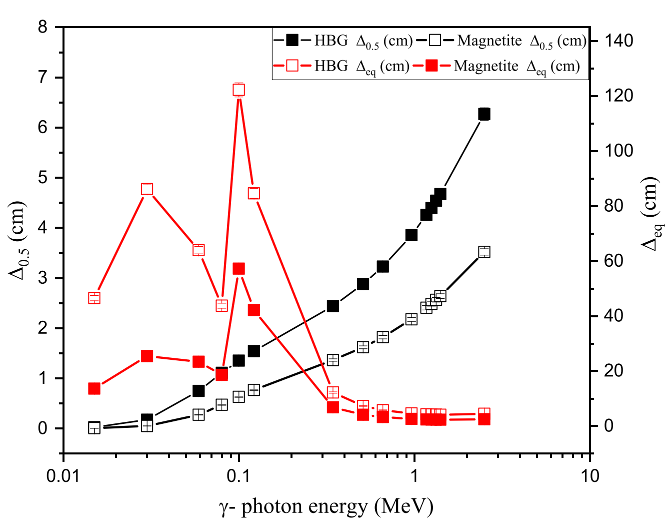

Fig. 6. Variation of the equivalent thickness (Δ_{eq}, cm) and the half value thickness ($\Delta_{0.5}$, cm) versus the γ-photon energy (MeV).

4. Conclusion

The different image analysis techniques such as PCA, band ratio, and MNF were applied over Hyperion data and found to be promising results in the discrimination of rock types of the study area. The band combinations 15, 31, and 47 were found highly efficient in enhancing the iron ore deposits of the study area. Compared to PCA and band ratio methods the results from the MNF method (5, 9, 2) are superior which accurately differentiated the boundary of each litho type. The spectral profiles generated from the Hyperion data corresponding to the lithologies of the region produced comparable results with the spectra taken from the laboratory conditions. Spectral features in the VNIR range of the spectrum are mainly caused by transition metals and a large number of Fe absorption regions were identified in the iron ore spectra retrieved from Hyperion data. The processing results were validated concerning field checks, published geology maps, and geochemical data of the study area. The image processing results and spectral characterization taken into the consideration for the present study are promising for the discrimination of lithologies of the Chelannur region. The μm suffers a high reduction in the width

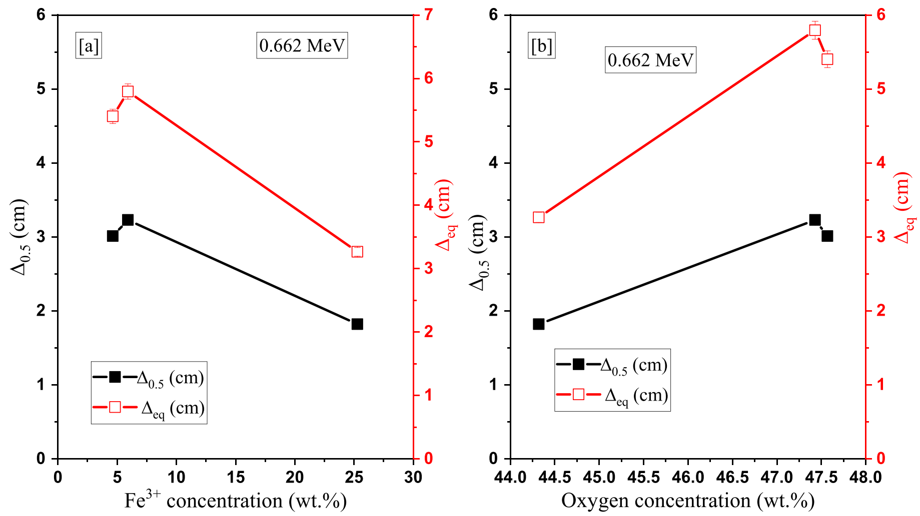

Fig. 7. Dependence of the equivalent thickness (Δ_{eq}, cm) and the half value thickness ($\Delta_{0.5}$, cm) versus the Fe^{3+} and oxygen concentration (wt.%).

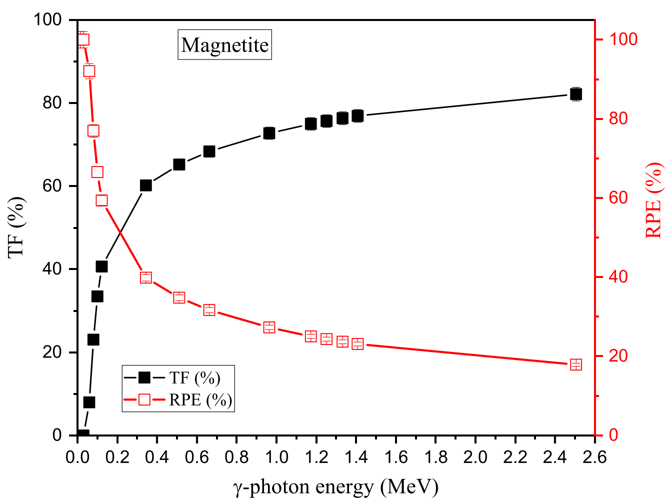

Fig. 8. Dependence of the transmission factor (TF, %) and the radiation protection efficiency (RPE, %) versus the γ-photon energy (MeV).

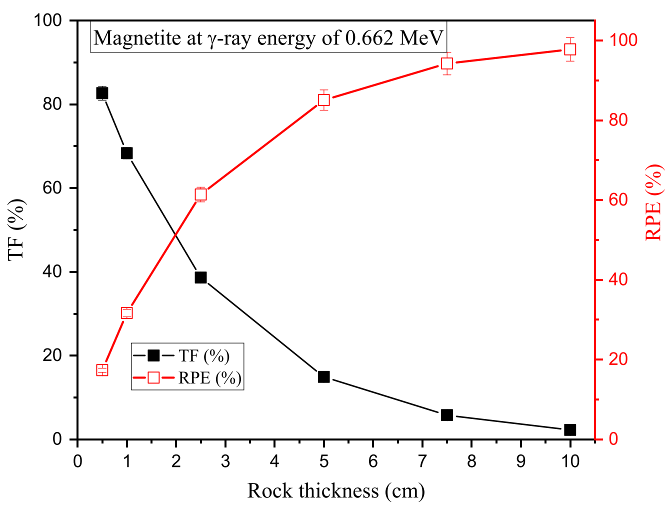

Fig. 9. Dependence of the transmission factor (TF, %) and the radiation protection efficiency (RPE, %) versus the rock thickness (cm).

raising the photon energy due to the PE cross-section that varies inversely with $E_{\gamma}^{3.5}$. In the mentioned energy interval, the μm loses approximately about 98.3 5 % (for HBS), 99.0 % (for Magnetite), and 98.3 % (for Charnockite), when the γ-photon energy increased from 0.015 to 0.122 MeV. The results show an enhancement of the μ values with raising the Fe^{3+} concentrations. The mentioned enhancement is approximately about 63.4 %, 43.6 %, and 43.5 % at E_{γ}values of 0.059, 0.662, and 1.25 MeV, respectively. Raising the oxygen ions causes a significant decrease in the μ values of the studied rocks which is accompanied by an increase in $\Delta_{0.5}$ and Δ_{eq} values. The $\Delta_{0.5}$ and Δ_{eq} values increased by factors of approximately 77 % with raising the oxygen ions between 44.32 and 47.57 wt.%.

Declaration of competing interest

The authors declare that they have no known competing financial interests or personal relationships that could have appeared to influence the work reported in this paper.

Acknowledgment

This work was supported by the King Khalid University through a grant RCAMS/KKU/03-22 under the Research Center for Advance Materials (RCAMS) at King Khalid University, Saudi Arabia.

References

[1] S.S. Obaid, D.K. Gaikwad, P.P. Pawar, Determination of gamma ray shielding parameters of rocks and concrete, Radiat. Phys. Chem. 144 (2018) 356–360, https://doi.org/10.1016/j.radphyschem.2017.09.022.
[2] F.I. El-Agawany, N. Ekinci, K.A. Mahmoud, S. Sarıtaş, B. Aygün, E.M. Ahmed, Y.S. Rammah, Gamma-ray shielding capacity of different B4C-, Re-, and Ni-based superalloys, Eur. Phys. J. Plus. 136 (2021) 527, https://doi.org/10.1140/epjp/s13360-021-01498-6.
[3] C. Aksoy, The X-Ray fluorescence parameters and radiation shielding efficiency of silver doped superconducting alloys, Radiat. Phys. Chem. 186 (2021), 109543, https://doi.org/10.1016/j.radphyschem.2021.109543.
[4] G. ALMisned, G. Kilic, E. Ilik, S.A.M. Issa, H.M.H. Zakaly, A. Badawi, U.G. Issever, H.O. Tekin, A. Ene, Structural characterization and gamma-ray attenuation properties of rice-like α-TeO_2 crystalline microstructures (CMS) grown rapidly on free surface of tellurite-based glasses, J. Mater. Res. Technol. 16 (2022) 1179–1189, https://doi.org/10.1016/j.jmrt.2021.12.059.
[5] G. ALMisned, H.O. Tekin, H.M.H. Zakaly, S.A.M. Issa, G. Kilic, H.A. Saudi, M. Algethami, A. Ene, Fast neutron and gamma-ray attenuation properties of some HMO tellurite-tungstate-antimonate glasses: impact of Sm^{3+} ions, Appl. Sci. 11 (2021), 10168, https://doi.org/10.3390/app112110168.
[6] H.M. Zakaly, A. Ashry, A. El-Taher, A.G.E. Abbady, E.A. Allam, R.M. El-Sharkawy,

M.E. Mahmoud, Role of novel ternary nanocomposites polypropylene in nuclear radiation attenuation properties: in-depth simulation study, Radiat. Phys. Chem. 188 (2021), 109667, https://doi.org/10.1016/j.radphyschem.2021.109667.
[7] F. Akman, H. Ogul, I. Ozkan, M.R. Kaçal, O. Agar, H. Polat, K. Dilsiz, Study on gamma radiation attenuation and non-ionizing shielding effectiveness of niobium-reinforced novel polymer composite, Nucl. Eng. Technol. (2021), https://doi.org/10.1016/j.net.2021.07.006.
[8] G. Kilic, E. Ilik, S.A.M. Issa, B. Issa, U.G. Issever, H.M.H. Zakaly, H.O. Tekin, Fabrication, structural, optical, physical and radiation shielding characterization of indium (III) oxide reinforced $85TeO_2$-(15−x)ZnO-xIn_2O_3 glass system, Ceram. Int. 47 (2021) 27305–27315, https://doi.org/10.1016/j.ceramint.2021.06.152.
[9] H.O. Tekin, G. Bilal, H.M.H. Zakaly, G. Kilic, S.A.M. Issa, E.M. Ahmed, Y.S. Rammah, A. Ene, Newly developed vanadium-based glasses and their potential for nuclear radiation shielding aims: a Monte Carlo study on gamma ray attenuation parameters, Materials (Basel) 14 (2021) 3897, https://doi.org/10.3390/ma14143897.
[10] M.T. Teli, L.M. Chaudhari, S.S. Malode, Attenuation coefficients of 123 keV γ-radiation by dilute solutions of sodium chloride, Appl. Radiat. Isot. 45 (1994) 987–990, https://doi.org/10.1016/0969-8043(94)90166-X.
[11] B. Aygün, B. Alaylar, K. Turhan, E. Şakar, M. Karadayı, M.I.A. Al-Sayyed, E. Pelit, M. Güllüce, A. Karabulut, Z. Turgut, B. Alım, Investigation of neutron and gamma radiation protective characteristics of synthesized quinoline derivatives, Int. J. Radiat. Biol. 96 (2020) 1423–1434, https://doi.org/10.1080/09553002.2020.1811421.
[12] N.K. Libeesh, K.A. Naseer, S. Arivazhagan, A.F. Abd El-Rehim, K.A. Mahmoud, M.I. Sayyed, M.U. Khandaker, Advanced nuclear radiation shielding studies of some mafic and ultramafic complexes with lithological mapping, Radiat. Phys. Chem. 189 (2021), 109777, https://doi.org/10.1016/j.radphyschem.2021.109777.
[13] O. Agar, H.O. Tekin, M.I. Sayyed, M.E. Korkmaz, O. Culfa, C. Ertugay, Experimental investigation of photon attenuation behaviors for concretes including natural perlite mineral, Results Phys. 12 (2019) 237–243, https://doi.org/10.1016/j.rinp.2018.11.053.
[14] Q. Chen, K.A. Naseer, K. Marimuthu, P.S. Kumar, B. Miao, K.A. Mahmoud, M.I. Sayyed, Influence of modifier oxide on the structural and radiation shielding features of Sm^{3+}-doped calcium telluro-fluoroborate glass systems, J. Aust. Ceram. Soc. 57 (2021) 275–286, https://doi.org/10.1007/s41779-020-00531-8.
[15] G. Sathiyapriya, K.A. Naseer, K. Marimuthu, E. Kavaz, A. Alalawi, M.S. Al-Buriahi, Structural, optical and nuclear radiation shielding properties of strontium barium borate glasses doped with dysprosium and niobium, J. Mater. Sci. Mater. Electron. 32 (2021) 8570–8592, https://doi.org/10.1007/s10854-021-05499-0.
[16] P. Evangelin Teresa, K.A. Naseer, K. Marimuthu, H. Alavian, M.I. Sayyed, Influence of modifiers on the physical, structural, elastic and radiation shielding competence of Dy^{3+} ions doped Alkali boro-tellurite glasses, Radiat. Phys. Chem. 189 (2021), 109741, https://doi.org/10.1016/j.radphyschem.2021.109741.
[17] R. Divina, K.A. Naseer, K. Marimuthu, Y.S.M. Alajerami, M.S. Al-Buriahi, Effect of different modifier oxides on the synthesis, structural, optical, and gamma/beta shielding properties of bismuth lead borate glasses doped with europium, J. Mater. Sci. Mater. Electron. 31 (2020) 21486–21501, https://doi.org/10.1007/s10854-020-04662-3.
[18] E.E. Saleh, T.M. Mohammed, M.T. Hussien, Investigation of radiological parameters and their relationship with rock type from Hifan area, Yemen, J. Geochemical Explor. 214 (2020), 106538, https://doi.org/10.1016/j.gexplo.2020.106538.
[19] R.P. Gupta, Remote Sensing Geology, Springer Berlin Heidelberg, Berlin, Heidelberg, Heidelberg, 2003, https://doi.org/10.1007/978-3-662-05283-9.
[20] F.D. Van der Meer, H.M.A. Van der Werff, F.J.A. Van Ruitenbeek, C.A. Hecker, W.H. Bakker, M.F. Noomen, M. Van der Meijde, E.J.M. Carranza, J.B. de Smeth, T. Woldai, Multi- and hyperspectral geologic remote sensing: a review, Int. J. Appl. Earth Obs. Geoinf. 14 (2012) 112–128, https://doi.org/10.1016/j.jag.2011.08.002.
[21] J.S. Pearlman, P.S. Barry, C.C. Segal, J. Shepanski, D. Beiso, S.L. Carman, Hyperion, a space-based imaging spectrometer, IEEE Trans. Geosci. Remote Sens. 41 (2003) 1160–1173, https://doi.org/10.1109/TGRS.2003.815018.
[22] H. Saibi, M. Bersi, M.B. Mia, N.M. Saadi, K.M.S. Al Bloushi, R.W. Avakian, Applications of remote sensing in geoscience, Recent Adv. Appl. Remote Sens. (2018), https://doi.org/10.5772/intechopen.75995.
[23] P.T.R. Chacko, Structure and Origin of the Iron Ore Occurrences Around Calicut Kerala State India, University of Kerala, 1977.
[24] N.K. Libeesh, K.A. Naseer, S. Arivazhagan, A.F.A. El-Rehim, G. ALMisned, H.O. Tekin, Characterization of Ultramafic–Alkaline–Carbonatite complex for radiation shielding competencies: an experimental and Monte Carlo study with lithological mapping, Ore Geol. Rev. 142 (2022), 104735, https://doi.org/10.1016/j.oregeorev.2022.104735.
[25] N.K. Libeesh, K.A. Naseer, S. Arivazhagan, K.A. Mahmoud, M.I. Sayyed, M.S. Alqahtani, E.S. Yousef, Multispectral remote sensing for determination the Ultra-mafic complexes distribution and their applications in reducing the equivalent dose from the radioactive wastes, Eur. Phys. J. Plus. 137 (2022) 267, https://doi.org/10.1140/epjp/s13360-022-02473-5.
[26] S. Arivazhagan, S. Anbazhagan, ASTER data analyses for lithological discrimination of sittampundi anorthositic complex, southern India, Geosci. Res. 2 (2017), https://doi.org/10.22606/gr.2017.23005.
[27] F. Janekovi, T. Novak, PCA – a powerful method for analyze ecological niches, Princ. Compon. Anal. - Multidiscip. Appl. (2012), https://doi.org/10.5772/38538.
[28] A. Sengupta, M. Das Adhikari, S. Maiti, S.K. Maiti, P. Mahanta, S. Bhaumick, Identification and mapping of high-potential iron ore alteration zone across Joda, Odisha using ASTER and EO-1 hyperion data, J. Spat. Sci. 64 (2019) 491–514, https://doi.org/10.1080/14498596.2018.1485120.
[29] R. Manuel, M. da G. Brito, M. Chichorro, C. Rosa, Remote sensing for mineral exploration in central Portugal, Minerals 7 (2017) 1–30, https://doi.org/10.3390/min7100184.
[30] A.F.H. Goetz, Imaging spectrometry for Earth remote sensing, Imaging Spectrosc. 228 (1992) 1–19.
[31] M. Sgavetti, L. Pompilio, S. Meli, Reflectance spectroscopy (0.3-2.5 μm) at various scales for bulk-rock identification, Geosphere 2 (2006) 142–160, https://doi.org/10.1130/GES00039.1.
[32] N.K.N.K. Libeesh, S. Arivazhagan, Satellite data based abundance mapping of mafic and ultramafic rocks in Mettupalayam, Tamil Nadu, India, Geol. Geophys. Environ. 47 (2021) 131–142, https://doi.org/10.7494/geol.2021.47.3.131.
[33] R.N. Clark, T.V.V. King, M. Klejwa, G.A. Swayze, N. Vergo, High spectral resolution reflectance spectroscopy of minerals, J. Geophys. Res. 95 (1990), 12653, https://doi.org/10.1029/JB095iB08p12653.
[34] A. Sengupta, M. Das Adhikari, S. Maiti, S.K. Maiti, P. Mahanta, S. Bhaumick, Identification and mapping of high-potential iron ore alteration zone across Joda, Odisha using ASTER and EO-1 hyperion data, J. Spat. Sci. 64 (2019) 491–514, https://doi.org/10.1080/14498596.2018.1485120.
[35] S. Arivazhagan, K.A. Naseer, K.A. Mahmoud, K.V. Arun Kumar, N.K. Libeesh, M.I. Sayyed, M.S. Alqahtani, E.S. Yousef, M.U. Khandaker, Gamma-ray protection capacity evaluation and satellite data based mapping for the limestone, charnockite, and gneiss rocks in the Sirugudi taluk of the Dindigul district, India, Radiat, Phys. Chem. 196 (2022), 110108, https://doi.org/10.1016/j.radphyschem.2022.110108.
[36] S. Arunkumar, K.A. Naseer, M. Yoosuf Ameen, K.A. Mahmoud, M.I. Sayyed, K. Marimuthu, D. James Silvia, R. Divina, M.S. Alqahtani, E.S. Yousef, Physical, structural, optical, and radiation screening studies on Dysprosium ions doped Niobium Bariumtelluroborate glasses, Radiat. Phys. Chem. 204 (2023), 110669, https://doi.org/10.1016/j.radphyschem.2022.110669.
[37] S. Arivazhagan, K.A. Naseer, K.A. Mahmoud, K.V. Arun Kumar, N.K. Libeesh, M.I. Sayyed, M.S. Alqahtani, E.S. Yousef, M.U. Khandaker, Gamma-ray protection capacity evaluation and satellite data based mapping for the limestone, charnockite, and gneiss rocks in the Sirugudi taluk of the Dindigul district, India, Radiat, Phys. Chem. 196 (2022), 110108, https://doi.org/10.1016/j.radphyschem.2022.110108.
[38] N.K. Libeesh, K.A. Naseer, K.A. Mahmoud, M.I. Sayyed, S. Arivazhagan, M.S. Alqahtani, E.S. Yousef, M.U. Khandaker, Applicability of the multispectral remote sensing on determining the natural rock complexes distribution and their evaluability on the radiation protection applications, Radiat. Phys. Chem. 193 (2022), 110004, https://doi.org/10.1016/j.radphyschem.2022.110004.
[39] M.I. Sayyed, N. Dwaikat, M.H.A. Mhareb, A.N. D'Souza, N. Almousa, Y.S.M. Alajerami, F. Almasoud, K.A. Naseer, S.D. Kamath, M.U. Khandaker, H. Osman, S. Alamri, Effect of TeO2 addition on the gamma radiation shielding competence and mechanical properties of boro-tellurite glass: an experimental approach, J. Mater. Res. Technol. 18 (2022) 1017–1027, https://doi.org/10.1016/j.jmrt.2022.02.130.
[40] M.I. Sayyed, M.K. Hamad, M.H. Abu Mhareb, K.A. Naseer, K.A. Mahmoud, M.U. Khandaker, H. Osman, B.H. Elesawy, Impact of modifier oxides on mechanical and radiation shielding properties of B_2O_3-SrO-TeO_2-RO glasses (where RO = TiO_2, ZnO, BaO, and PbO), Appl. Sci. 11 (2021), 10904, https://doi.org/10.3390/app112210904.
[41] K.A. Naseer, K. Marimuthu, K.A. Mahmoud, M.I. Sayyed, Impact of Bi_2O_3 modifier concentration on barium–zincborate glasses: physical, structural, elastic, and radiation-shielding properties, Eur. Phys. J. Plus. 136 (2021) 116, https://doi.org/10.1140/epjp/s13360-020-01056-6.
[42] S.A. Bassam, K.A. Naseer, V.K. Keerthana, P. Evangelin Teresa, C.S. Suchand Sangeeth, K.A. Mahmoud, M.I. Sayyed, M.S. Alqahtani, E. El Shiekh, M.U. Khandaker, Physical, structural, elastic and optical investigations on Dy^{3+} ions doped boro-tellurite glasses for radiation attenuation application, Radiat. Phys. Chem. (2023), 110798, https://doi.org/10.1016/j.radphyschem.2023.110798.
[43] M.U. Khandaker, D.A. Bradley, H. Osman, M.I. Sayyed, A. Sulieman, M.R.I. Faruque, K.A. Naseer, A.M. Idris, The significance of nuclear data in the production of radionuclides for theranostic/therapeutic applications, Radiat. Phys. Chem. 200 (2022), 110342, https://doi.org/10.1016/j.radphyschem.2022.110342.
[44] S. Yasmin, M.U. Khandaker, D.A. Bradley, H. Osman, A. Alyahyawi, M.I. Sayyed, M.R.I. Faruque, K.A. Naseer, A.M. Idris, The efficacy of various thicknesses of float glasses for protection of gamma-radiation, Radiat. Phys. Chem. 199 (2022), 110301, https://doi.org/10.1016/j.radphyschem.2022.110301.
[45] D.A. Aloraini, M.Y. Hanfi, M.I. Sayyed, K.A. Naseer, A.H. Almuqrin, P. Tamayo, O.L. Tashlykov, K.A. Mahmoud, Design and gamma-ray attenuation features of new concrete materials for low- and moderate-photons energy protection applications, Materials (Basel) 15 (2022) 4947, https://doi.org/10.3390/ma15144947.